1 Radiation Environment

(**** this section is supposed to be 1.3.3, subsections correspondingly ****)

1.1 Overview

The nominal luminosity of LHC, 10^{34} cm^{-2} s^{-1} together with the 7 TeV beam energy, will create a very hostile radiation environment which all subdetectors will have to deal with. It has been known since the first LHC pre-studies, that the inner tracker and very forward calorimeters of LHC experiments will be confronted with unprecedented radiation levels. Later it has been shown that also the endcap calorimeters and the muon spectrometer will suffer from the environment. In CMS, due to the strong solenoidal field and the massive iron yoke, the barrel calorimetry and barrel muon spectrometry are least affected by background and radiation damage effects.

We can distinguish three regions with quite different characteristics from the shielding point of view.

1. The main detector, up to η=3.0, where we have to deal with the pp-secondaries directly, but also with neutron albedo and hadronic punchthrough.
2. The region η=3.0-5.3 is covered by the HF. Cascades developing here affect the HF itself and its electronics, but any leakage would be of concern for the close by endcap muon system also.
3. At pseudorapidities beyond the acceptance of the HF comes the collimator, which protects the superconducting quadrupoles. Cascading in this region is the dominant source of radiation background in the experimental cavern outside of the detector.

Particles with $\eta > 7.9$ will not be captured in the experimental area.

The fact that radiation issues have become increasingly important with the high energy hadron colliders might lead to the erroneous conclusion that the higher energies alone cause the problems. In fact most of the radiation issues, except punchthrough, are connected with low energy phenomena, which are the same at almost all hadron accelerators. Compared to existing hadron colliders, the high beam energy of LHC increases the particle multiplicities and the total amount of energy deposited, but much more important is the extremely high luminosity. Together they result in numerous intense cascades, which all end up in an immense number of low energy particles. Therefore the radiation studies have to focus on the energy range around 1 GeV and below. Particle energies exceeding 10 GeV are very rare in the minimum bias background.

1.1.1 Radiation damage

The hostile radiation environment implies that a lot of attention has to be devoted to selecting sufficiently radiation hard technologies. A significant part of LHC related R&D work has in fact concentrated on radiation hardness studies of detectors and electronics.

Silicon devices will be used in essentially all parts of CMS, either as electronic chips, as charged particle detectors or as photodiodes.

Properties of bulk silicon are significantly degraded by displacement damage effects, i.e. distortions of the crystal structure. Such defects can be introduced only as a result of relatively large energy transfers to lattice atoms. Therefore electrons and photons cause almost no bulk damage in silicon. Hadrons,

however, can transfer large amounts of energy to the lattice atoms either in elastic or inelastic collisions. Part of this energy is distributed as non-ionizing energy loss, which results in a large number of lattice defects. To a reasonable approximation the amount of bulk damage depends on the collision cross section for a given particle weighted by the average energy transfer in a collision. For low energy neutrons the cross section is relatively large, but energy transfers are moderate, whereas for fast hadrons the small cross section is compensated by a larger average energy transfer per collision. Experimental results have verified the simulations, according to which all hadrons induce roughly the same damage in silicon per unit fluence. This has one important exception: neutrons below 100 keV, for reasons of kinematics and energy behaviour of cross sections, induce only very little damage and usually they are not considered at all when estimating bulk damage in silicon. Since the non-ionizing energy loss is a very small fraction of the total dE/dx of a charged particle - and since this fraction is almost zero for electrons, bulk damage has essentially no relationship to radiation dose.

Completely independent of the bulk damage we can also observe surface damage effects in silicon. These are especially important for electronics components. Surface damage is related to trapped charge in oxide layers. Since this charge is generated by the passage of a charged particles, surface damage can be observed also for electron and photon irradiation. While bulk damage is related to the hadron fluence, surface damage appears to be a function of radiation dose.

Similar dose-related damage effects have been reported for organic and inorganic scintillators, i.e. the $PbWO_4$ crystals of the CMS electromagnetic calorimeter and the plastic scintillators of the CMS central hadron calorimeter. In these cases the light transmission degrades due to the generation of color centers by the ionization(**** also for plastic, HCAL people please verify ??? ****). Thus the degradation of scintillators is also a function of the radiation dose.

Although in most cases significant annealing is observed, some fraction of the damage is never recovered and the detectors continuously degrade with increasing fluence or dose.

The annealing effects make radiation damage a complicated function of both time and fluence. For instance the calibration of a calorimeter might change due to both, degradation during irradiation and simultaneous improvement due to annealing. If the annealing is very fast the calorimeter response can become luminosity dependent.

For bulk damage of silicon detectors so called reverse annealing is observed. In this case detectors which have been exposed to a sufficiently high fluence continue to degrade even without any further irradiation. Although this reverse annealing can be slowed down by lowering the temperature, it still means that detector life time is not determined by accumulated fluence alone, but also by the actual time over which this accumulation is done.

1.1.2 Background effects

Radiation is also connected with increased signal occupancy of detectors. Some fraction of the radiation background is always included in the standard detector simulations and usually referred to as minimum bias background, which might give the wrong impression that there is nothing else on top of it.

In reality normal detector simulations usually do not include low energy neutron transport which usually ends up in neutron capture and subsequent photon emission. These photons, like secondaries from other low energy effects like pion capture, neutron induced nuclear reactions and nuclear fragmentation, can add up to a significant fraction of the total radiation background. In addition to all high energy phenomena, these low energy effects are fully accounted for in the dedicated radiation environment simulations.

The neutron background, which in fact should be called photon or low energy background in order to emphasize its true effect on detectors, is important in regions where other ionizing radiation is strongly suppressed. In CMS such regions are especially the whole muon spectrometer, where 50% to almost 100% of the signals are caused by these low energy phenomena.

1.1.3 Induced radioactivity

While induced radioactivity is negligible at electron-positron colliders, it will be a major concern at LHC. We can assume that each inelastic hadronic interaction results in a residual nucleus, which can be almost anything below the target mass and charge. This residual can directly end up being stable, but more probably it will be radioactive.

Only some 30% of the interactions lead to formation of long-lived radionuclides, which we would really see as induced activity when entering the area. But this activity decreases relatively slowly after the end of irradiation, so that even long cooling times do not significantly improve the situation. A rough rule of thumb is that the effective half life of the remaining radioactivity is equal to the time, which has elapsed after the end of irradiation.

But safety aspects are not necessarily the whole issue connected with induced activity. None of the simulation codes used for the radiation environment studies considers the radioactive decay of the very short-lived residual nuclides. Although these are insignificant for safety, they will emit photons, which can increase the background. Locally this increase cannot be large, because the saturation activity always will be only a small fraction of the activating flux, which usually itself generates a signal. Therefore β-emission should not be an issue, except if it is caused by neutron activation. But photons can travel large distances, so that a highly activated object, for instance the beam pipe, can lead to increased background elsewhere.

1.1.4 Shielding requirements and materials

Inside of CMS shielding is dictated by the very limited space available. Therefore materials have been selected to provide the most efficient shielding in the smallest amount of space. An equally strong constraint to the choice of shielding strategy arises from the fact that the performance of the detectors cannot be jeopardized.

Outside of the detector, around and beyond the HF, the constraints come mainly from cost and weight, although space restrictions have to be also taken into account for the HF shielding.

At LHC we are confronted with a radiation environment which includes essentially all types of particles. The energy distribution ranges from thermal neutrons up to the typical hadron energy around 1 GeV and ends in a high energy tail which extends to few TeV. This heterogeneous radiation environment implies that no shielding material alone will be the perfect one.

Shielding of pure electromagnetic radiation is the simplest case, any high-Z material does a good job and lead is the usual choice. At LHC the problem with photon shielding is, that introduction of lead or other high mass material in a high-energy hadron environment leads to excessive production or secondary neutrons. So one often has to find a compromise between suppression of the, in principle harmless, neutron flux and the often more harmful photon flux.

For high energy hadrons the shielding performance depends on the interaction length, which to first approximation depends on the atomic density, but has also a $A^{0.7}$ dependence on the atomic mass number

A. Metals, like iron or copper, have typically mean free paths around 15-20 cm, tungsten even below 10 cm, but aluminium almost 40 cm. The common choice for shielding against high energy hadrons is iron, mainly due to its relatively low price. If normal concrete (density 2.35 g/cm^3) is used, about 2.5 times the iron thickness is needed. Several concretes with heavy aggregates, reaching densities up to 4.5 g/cm^3, can be produced. In CMS magnetite concrete with a density of 3.65 g/cm^3 is considered as the baseline. Except for the proposed boron content, this magnetite concrete is roughly equivalent to normal concrete containing iron reinforcements to achieve the same density.

Neutron shielding is the most complicated case, in particular since there are correlations with photon shielding as indicated above, but also with the shielding against fast hadron (including fast neutrons). It is, in fact, the presence of the fast hadrons, which makes the LHC radiation environment very different from that encountered at nuclear reactors.

As a general rule neutrons have to be first slowed down to thermal energies so that their capture cross section increases. This slowing down is best achieved by moderators containing as much hydrogen as possible. The most common choice is polyethylene. As far as silicon damage is concerned slowing down the neutrons is already sufficient, since a slow neutron is almost harmless. At neutron energies above few MeV hydrogen starts to lose its efficiency. At these energies inelastic interactions start to dominate and the neutrons behave like fast hadrons and are best attenuated by heavy absorbers.

But when we consider activation by low energy neutrons or, especially, background effects due to the capture photons, the situation is much more complicated. There are a few materials which are commonly used to get rid of the thermal neutrons. The most efficient one is cadmium, but it has the severe drawback of producing numerous energetic capture photons. A more suitable neutron capturer is boron, which can be easily admixed to polyethylene. In addition to suppressing efficiently the thermal neutron flux, it has the advantage of competing with hydrogen on the neutron capture. Thus most of the 2.2 MeV capture photons from hydrogen are replaced with 470 keV photons from boron. But due to the higher capture cross section there will be more of these boron capture photons, which still are energetic enough to require some shielding between the borated polyethylene and any sensitive volume. Lithium is the third material which can be used to suppress thermal neutrons. It is almost unique in not producing any capture photons. But in addition to a lower cross section than boron, it has the drawback that the effective isotope ^{6}Li is contained only to a fraction of 7.5% in natural lithium.

Doping of polyethylene, whether with boron or lithium, should be carefully considered, since it will not only increase the price but also lower the relative hydrogen content. Thus the efficiency in slowing down the neutrons will be degraded to achieve suppression of thermal neutrons, which is not always even needed. In addition, as indicated above, the addition of boron significantly increases the probability of neutron capture and so can increase the photon background compared to pure polyethylene or no polyethylene at all. On the other hand such effects are only local. In an essentially closed system, like the CMS experimental area, every neutron will be captured sooner or later, and it is of advantage to have this happening in a controlled way in predefined material. Therefore borated polyethylene layers are proposed around essentially all of the forward shielding, but in the immediate vicinity of sensitive detectors they are avoided or backed up with photon absorber.

1.2 LHC parameters

1.2.1 Luminosity

The usually quoted LHC luminosity of 10^{34} cm^{-2}s^{-1} is in fact the value at the beginning of the fill when the machine is operating at its nominal parameters. During the fill the beam intensity goes down due to

various loss processes and the luminosity decreases correspondingly. No final decision on the number of fills per day has been taken, but it has been shown that about the same day-averaged luminosity can be reached with either one or two fills. In both cases this average is roughly half of the nominal value [1].

1.2.2 Assumed operation schedule

For the assessment of radiation effects we need to consider both the integrated fluence or dose and the instantaneous flux or dose rate. Which of the two is appropriate depends on the detector type and the expected radiation effects. Detector occupancies, for instance, depend only on the instantaneous particle rate, whereas radiation damage is often a cumulative effect. For the estimation of induced activity even differences in the irradiation histories have to be considered. This is due to the fact that residual nuclides are produced proportionally to the integrated luminosity, but the decay of radioactive isotopes takes place simultaneously and, for a given nuclide, is only a function of time.

As pointed out earlier, a similar situation is found in radiation damage if annealing effects play an important role. Therefore integrated fluences and doses are often not sufficient to estimate radiation damage effects, but an assumption of the machine schedule has to be included in the calculations.

Following the suggestion of [2], we assume three periods of 60 days pp operation per year. These periods would be separated by ten day shutdowns in between. Following a 17 day shutdown could come a heavy-ion operation period of 6 weeks.

The nominal CMS program foresees the accumulation of an integrated luminosity of 5×10^5 pb^{-1}. Under the above assumptions for the operating conditions 0.78×10^5 pb^{-1} can be integrated per year. Taking into account that during the first three years we expect to integrate roughly the same amount as during one year of nominal luminosity operation, 5×10^5 pb^{-1} will be reached during the eighth calendar year at the earliest.

1.2.3 Heavy ion operation

Heavy ion operation is foreseen for a relatively short period per year. Tentatively 6 weeks have been suggested [2]. The peak luminosity in the Pb-Pb mode will be 1.95×10^{27} cm^{-2} s^{-1}. Compared to the proton-proton operation, the inelastic cross section and the average multiplicity are expected to be larger by factors of about 35 and 200, respectively. Even so, the average background from Pb-Pb-operation remains about three orders of magnitude below that of the high luminosity proton-proton collision mode. The instantaneous particle rate resulting from a central Pb-Pb collision, however, will be about 50 times larger than for an average proton-proton bunch crossing.

1.3 Event generators

1.3.1 Minimum bias events

The radiation environment simulations are based on minimum bias events obtained from the DPMJET-II event generator [3]. DPMJET-II is the most recent of the Dual Parton Model generators, which are specially suited for simulation of minimum bias hadronic collisions. As one of the updates with respect to the best-known of its predecessors, the DTUJET93 generator [4], DPMJET-II includes a complete description of charm production.

η=0.0-3.0 Main detector	η=3.0-5.3 HFs	η=5.3-7.9 Collimators	$\eta >$7.9 Leaving area
100 GeV	760 GeV	4480 GeV	8660 GeV

Table 1: Average energy distribution of inelastic minimum bias events into different pseudorapidity regions according to predictions from the DPMJET-II event generator.

The global scaling parameter for the radiation levels at LHC is the inelastic interaction rate, which is defined by the luminosity discussed above and by the inelastic cross section. For the latter a value of 80 mb will be assumed. This includes a sizeable fraction of diffractive events. Double diffraction is a relatively rare process and as far as the radiation environment is concerned it will be essentially equivalent to normal inelastic collisions. Some 15 percent of the collisions are expected to be single diffractive. In these events the other participating proton continues with only a small sideways deflection, much like in elastic scattering. Therefore only the dissociated proton contributes to the radiation background in the experimental area.

To get a rough idea how energy is distributed in the experimental area, we can analyze the angular distribution of the particles emerging from the generated minimum bias events. Tab. 1 shows the energy distribution of the DPMJET-II events into different η regions. The effects of decays and the magnetic field have not been taken into account.

1.3.2 High p_T events

The 4T solenoidal field combined with the massive barrel calorimetry and the iron yoke of CMS, leads to a strong suppression of soft background in outer barrel detectors. Thus, even though they are associated with low cross sections, decays of heavy flavours leading to high transverse momenta might not be totally negligible. Although DPMJET-II takes care of charm, it is expected that the production cross section for b-quarks is of the order of 0.35 mb. This is just at the limit of being potentially important for the outer barrel muon spectrometer. Although certainly of no significance for the inner and forward detectors, it was decided to include b-events in all the simulations. This ensures a coherent basis for the radiation environment simulations of all CMS subdetectors.

Events containing b-quarks were extracted from PYTHIA [5] and added to the minimum bias events from DPMJET-II. These b-events are not included in Tab. 1 but due to the small cross section, 0.35 mb as opposed to the 80 mb of the minimum bias events, they would not change the numbers within the accuracy with which these are given.

1.3.3 Event sampling

The minimum bias event file includes 2000 events and the b-event file 500. Both files have been randomized, i.e. the secondaries have been randomly reordered neglecting the event structure. The average total multiplicity per event is 124.

(**** do we keep following paragraph in TDR ? ****)

After the event structure has been destroyed by the randomization procedure, studies at the single event level are not possible. But these are not important, since the 25 ns bunch spacing of LHC is insignificant for the radiation background in the CMS system. Using randomized files energy conservation is possible

only on average. Also this is no limitation, since a significant random fraction of the energy leaves the CMS area through the collimator opening (Tab. 1) and the variance reduction techniques, to be discussed below, allow only average energy conservation, anyway. Compared to an event-by-event file the randomized file provides a smoother source and more flexible possibilities in determining the batch size in the simulations.

The scaling of the obtained results to some integrated LHC luminosity is then based on the assumed interaction cross section and on the average multiplicity in the event files.

In order to increase the sampling statistics for the rare b-events a weighted scheme was used: every tenth secondary was taken from the b-event file. The corresponding physical fraction arising from average multiplicities and cross sections would be only 1.1 percent. The difference is compensated by adjusting the statistical importance of the particles.

1.4 Simulation methods

1.4.1 Radiation transport codes

The radiation simulations are independent from the general detector performance simulations and are performed with simulations codes, which are specially designed for radiation physics. FLUKA [6] is the baseline code for the radiation environment simulations of CMS, but MARS and GCALOR are also used for various dedicated studies.

Although FLUKA does not provide a user friendly geometry interface like GCALOR and is therefore not compatible with CMSIM, its use is motivated by more accurate and up-to-date physics models and the indispensable variance reduction possibilities.

(**** following needed ???? ****)

The main features of FLUKA physics are: Generation of hadronic interactions from 20 MeV up to 20 TeV. Pre-equilibrium cascade model for inelastic interactions below 1.3 GeV and for capture reactions at rest. Nuclear evaporation and gamma de-excitation after inelastic interactions. Extended version of the EGS4 electromagnetic shower code [7]. Multigroup transport of neutrons below 20 MeV with detailed kinematics for (n,p) scattering and accounting for self shielding effects in some materials. Neutron capture reactions with explicit photon emission. Accurate multiple scattering and magnetic field transport even in thin layers. Full accounting for ionization loss, including latest parametrizations for the density effect at high energies and shell corrections at low energies. Transportable particles are all stable hadrons up to Ω, $e^{\pm}$, muons and photons.

1.4.2 General geometry description

A substantial effort has been devoted to finding the best parameters and approximations to describe the CMS system so that it remains feasible to implement with the geometry routines of FLUKA. Roughly 1000 volumes are needed to achieve this for the full CMS detector including shielding and the surrounding hall. Each detector has been described only with the minimum accuracy which was considered sufficient. For instance, the absorbers and active layers of HB and HE have been included explicitly in order to be fully sensitive to low energy neutron effects whereas the HF is described as a block of average material, since its fine structure is not expected to have an effect on the radiation levels.

A major approximation is that everything is assumed to have cylindrical symmetry. This is enforced by

the fact that even then it is difficult to collect sufficient statistics in all subdetectors. A deviation from cylindrical symmetry would change the quasi two-dimensional model to true three dimensions, which would prevent azimuthal averaging and so would considerably reduce the statistics in the simulations.

The geometry is terminated at a radius of 13 metres and a half-length of 27 metres. Thus 1 metre of the concrete walls at the ends and sides of the experimental hall are included in the simulations. This is more than sufficient to account for all radiation scattered back into the hall.

The magnetic field in the first low-β quadrupole, which resides partly within the geometry, is taken into account. The copper collimator is located at z=19.0-20.8 m and has an inner radius of 1.5 cm. It is surrounded by a fixed conical iron shield of 45-80 cm radial thickness. In run-time configuration this shield is enclosed in the rotating shielding, and during maintenance it fits into the opening in the endcap.

A complete description of the forward shielding is included in the simulations. Special emphasis has been put on the region around the forward calorimeter.

1.4.3 Energy cuts and transport parameters

The lower threshold for neutron transport was set to thermal energy. The thermal group of FLUKA ranges from 10^{-5} eV to 0.414 eV, but the mean thermal energy used to produce the 293 K group cross sections is 0.025 eV. Other hadrons, if not decaying, interacting or leaving the system, were ranged out to zero energy. But the threshold energy for the production of charged hadrons was set to 100 keV. Due to the short range at low energies this threshold is effectively the transport cut for charged hadrons. Antineutron transport was stopped at 50 MeV. Energy cuts for electromagnetic particles are more problematic, because of the intolerable increase of computing time if cuts are set too low. Therefore the energy thresholds for photon, electron and positron transport were adjusted according to the region. The absolute lower cut was 100 keV for electrons and 30 keV for photons, which was used in most of the sensitive detectors and their surroundings - including all of the air in the experimental area. In HCAL 300 keV was used for electrons and 100 keV for photons. In the HF cuts varied from 3 MeV to 100 keV for electrons and from 1 MeV to 30 keV for photons.

The full 2-dimensional (azimuthally symmetric) magnetic field map of CMS was used in the region of the main detector. Except for the first low-β quadrupole, the field was set to zero beyond z=10.8 m and r=6.95 m.

Multiple scattering was performed down to the Moliere limit. Delta electrons were produced above 100 keV to 10 MeV, depending on the material. Bremsstrahlung and pair production by high energy muons and charged hadrons were explicitly simulated.

1.4.4 Variance reduction methods

(**** this is all technical details, but a central feature of the calculations. So what to do ? ***)

In order to speed up convergence. i.e. to counteract the large attenuation in the shielding or other massive objects like calorimeters, different variance reduction methods have been used. The most important one is region importance biasing, where a certain direction of particle penetration is favoured by splitting or killing particles crossing predefined surfaces. In a pure attenuation problem this method can, ideally, transform the exponential dependence between shield thickness and computing time to a linear one. While region importance biasing is active only during transport, Russian roulette (killing randomly a fraction of the secondaries emerging from an interaction) is used to suppress the high particle number

in the core of cascades. An analogous role is played by leading particle biasing in electromagnetic interactions. Here only one, preferably the one with higher energy, of the two emerging particles is followed. The fourth biasing method used is decay length biasing, where the life time of mesons is decreased in order to improve statistics on muons.

All of the variance reduction methods described conserve four momentum and quantum numbers on average. This is achieved by adjusting the statistical weight of surviving or cloned particles. Thus, in a biased simulation, a particle does not represent a physical particle, but rather the probability of observing such a particle in a given region of phase space.

The gain in computing time comes from the fact that properly adjusted biasing tends to smooth the particle population across the entire phase space or even to decrease the population in regions of no interest.

1.4.5 Estimation of error margins

All simulations have been divided into several independent batches of equal size. These have been used to estimate the statistical errors arising from fluctuations in the event sampling and during cascade simulation. Only these statistical error estimates are indicated in the figures as 1 σ error bars.

A first uncertainty arises from the extrapolation of existing data to the inelastic proton-proton cross section at 14 TeV. A further uncertainty concerning the event multiplicities and momentum distributions comes on top of this. We should therefore expect an underlying uncertainty of about 30 percent from the pp-events alone [8] which probably cannot be reduced before LHC minimum bias data is available. This error is the dominant one as far as hadron fluxes at the CMS tracker are concerned. In all other regions uncertainties in the cascade development overwhelm this 30 percent.

The accuracy of the cascade simulation is affected by approximations in geometry description, incompleteness of physics models and cross section data sets.

FLUKA has been benchmarked in several small scale experiments using neutron counters and activation foils. The agreement with measurements is of the order of few tens of percent even after several attenuation lengths of shielding [9].

But these experiments corresponds to relatively simple and well defined target geometries with surrounding shielding blocks where all material compositions are rather well known. At CMS we can expect major uncertainties to arise from the modelling of the geometry and the assumptions made concerning material compositions. Probably the most reliable error estimate for these is obtained by repeating the simulations with different codes used by different groups. This should be seen less as a test the physics of the codes themselves, but more as a means to gather information on how much small differences in the geometry description affect the results. Inter-comparisons performed so far between FLUKA, MARS and GCALOR indicate that a factor of three should be a reasonable assumption for the overall uncertainty of the radiation levels in most parts of the CMS.

1.5 Barrel and endcap calorimeter

For technical reasons the FLUKA geometry model of the HB is a slightly adjusted version of the actual one. The HB is modelled to be perfectly symmetric, i.e. the tile structure and polygonal shape have not been taken into account. The scintillator is 0.82 cm thick, without any surrounding air. The scintillator density has been slightly reduced to restore the correct thickness of plastic. The absorber plates are

49.2 mm thick copper, except for the first and last which are stainless steel of 41 mm and 65.6 mm thickness, respectively. The HB starts at a radius of 193 cm and ends at 292.24 cm. In z-direction it is limited by the 53 degree cracks which separate it from the endcaps.

The 53 degree crack will house the cables and services of all inner subdetectors. A filling fraction of 30% is assumed and the material in the crack is averaged for the simulations. The cable bundles extend over the HE and then bend around the end of the coil and continue to the crack between barrel wheels YB0 and YB1.

Also for the HE perfect cylindrical symmetry is assumed. The scintillator thickness is taken to be 8.8 mm. The standard absorber plates are copper of 79.2 mm thickness. The HE starts at z=388 cm with a 17.2 mm thick scintillator layer and ends at z=555.56 cm. Starting at z=560 cm comes a 100 mm thick stainless steel plate. Radially the HE is limited by the η=3.0 line from below and by a maximum radius of 270 cm from above. In addition the 53 degree crack cuts a corner out of the HE.

Fig. 1 gives an overview of hadron (E> 100) fluence and radiation dose in the CMS HB/HE region. At the end of the HE we can see some radiation streaming in the 3.44 cm wide gap, which is caused only by the approximate geometry. This gap is not present in reality and we can see that at large radii it leads to slight overestimation of neutron fluence.

While Fig. 1 is based on data obtained with a binning which is much coarser than the internal structure of the calorimeter, Fig. 2 shows the dose in the HE for some fixed radii with a binning fitted to the internal structure. The alternation of absorber and scintillator layers in the HE becomes visible as a strong variation of the dose. This clearly indicates that a dose calculated in average material would underestimate the critical parameter, which is the dose in the plastic scintillators. Because most of the dose increase is due to recoil protons induced by low energy neutrons, simple corrections based on the variation of dE/dx cannot correct for the effect.

In Fig. 2 the effect of the calorimeter boundary at η=3 is becomes significant at the smallest radii. The increase of dose as a function of depth is due to the particles entering the calorimeter from its η=3 boundary. At the end of the HE the dose increase is caused by the slot for the muon station ME1/1 and the crack left in the simulation model between the HE and the stainless steel back plate.

1.6 Forward calorimeter

HF is exposed to the most intense radiation of all CMS subdetectors. This is best seen if we consider that on average 760 GeV per event are incident on the two forward calorimeters, compared to only 100 GeV for the whole main detector. In addition, this energy is not uniformly distributed, but has a pronounced maximum at the highest rapidities.

Aspects of concern for the HF will be the radiation damage of the quartz fibres, of the photomultipliers and of readout electronics. But we also have to consider the influence of the HF on other subdetectors, the endcap muon chambers in particular.

The quartz fibres themselves can sustain significant radiation doses and hadron fluences. The hadron fluence and dose profiles in the HF are shown in Fig. 3. The lower energy cut for plotting the hadron fluence, including neutrons, is 100 keV.

We can see from Fig. 3 that the shielding quite efficiently suppresses the hadron flux, and in particular the optimized interface between the endcap and the HF provides good shielding for the ME4 muon station. The polyethylene/iron layer around the back shielding plug protects the HF photomultipliers. The endplug efficiently suppresses both the dose and the neutron flux at the back of the calorimeter and

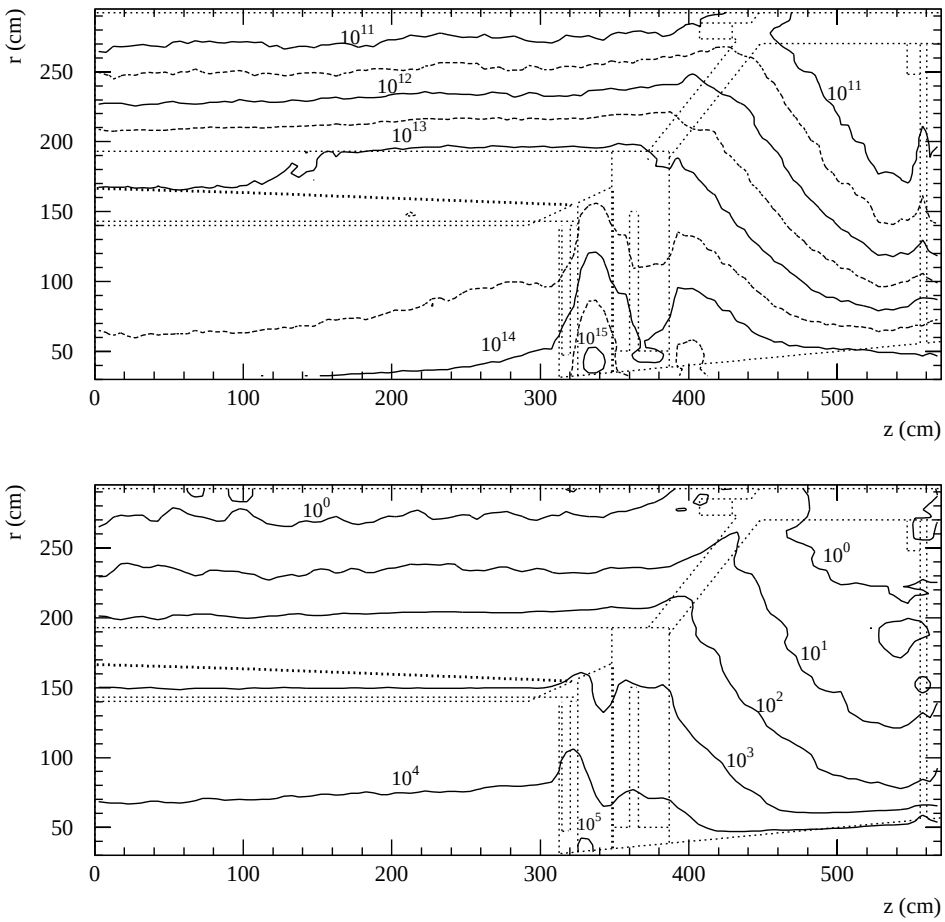

Figure 1: Fluence of hadrons (E>100 keV) in $\mathrm{cm}^{-2}\mathrm{s}^{-1}$ (upper plot) and radiation dose in Gy (lower plot) in the HB/HE region. The dose values have been smoothed by taking weighted running averages over neighbouring bins. Values are given for $5 \times 10^5\,\mathrm{pb}^{-1}$. The intermediate (dashed) contours in the fluence plot correspond to 3.16×10^n. The dotted lines indicate the geometry.

smoothly joins with the rotating shielding. The shielding around the HF is the most important one for ME4. We can see that it suppresses neutron fluence and dose below the overall levels in the experimental area.

1.7 Influence on other subdetectors

The main HCAL (HB/HE) is absorbing most of the 100 GeV of energy dissipated in the $\eta < 3$ region per event. Thus sufficiently thick HB and HE are important in order to reduce the hadronic background in the innermost muon stations. This is an especially critical issue for the most exposed endcap muon station ME1/1.

It can be seen from Fig. 1 that the $PbWO_4$ electromagnetic calorimeter, which will be in front of the

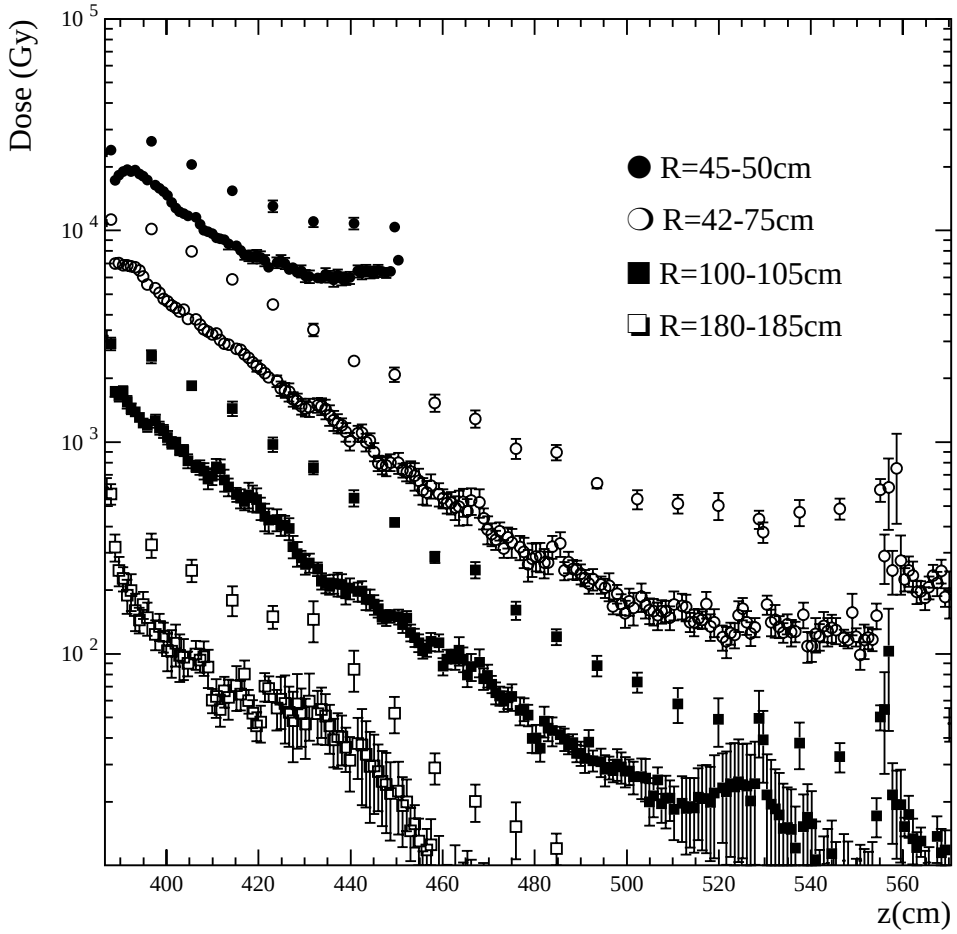

Figure 2: Radiation dose for 5×10^5 pb^{-1} at fixed radii in the endcap HCAL. The error bars indicate only the statistical error of the simulations. The points with higher dose correspond to energy deposition in the scintillator layers.

HCAL, is the dominant source of neutron fluence for both the inner tracker and its own readout electronics. In the endcap region the EE electronics, which is positioned in the gap between the EE and the HE, has to be first of all shielded against neutrons emerging from the EE itself. The neutron albedo from the HE into this gap is about a factor of two lower than the neutron fluence originating from the EE [10].

There will be some unavoidable leakage out from the $\eta = 3$ edge of the HE, which will contribute to the background in the endcap muon spectrometer.

It has been always recognized that if not shielded properly, the HF would significantly influence the radiation levels in other detector systems. Recently it has been shown that the central tracker would not suffer from any neutron albedo from the HF, even if it is completely unshielded [11]. But it is the endcap muon system which needs to be shielded against radiation leakage from HF. The muon chamber that is most affected is ME4, but also the high-η regions of other forward chambers require significant shielding in order to suppress the HF albedo. The full HF shielding is discussed in a dedicated chapter.

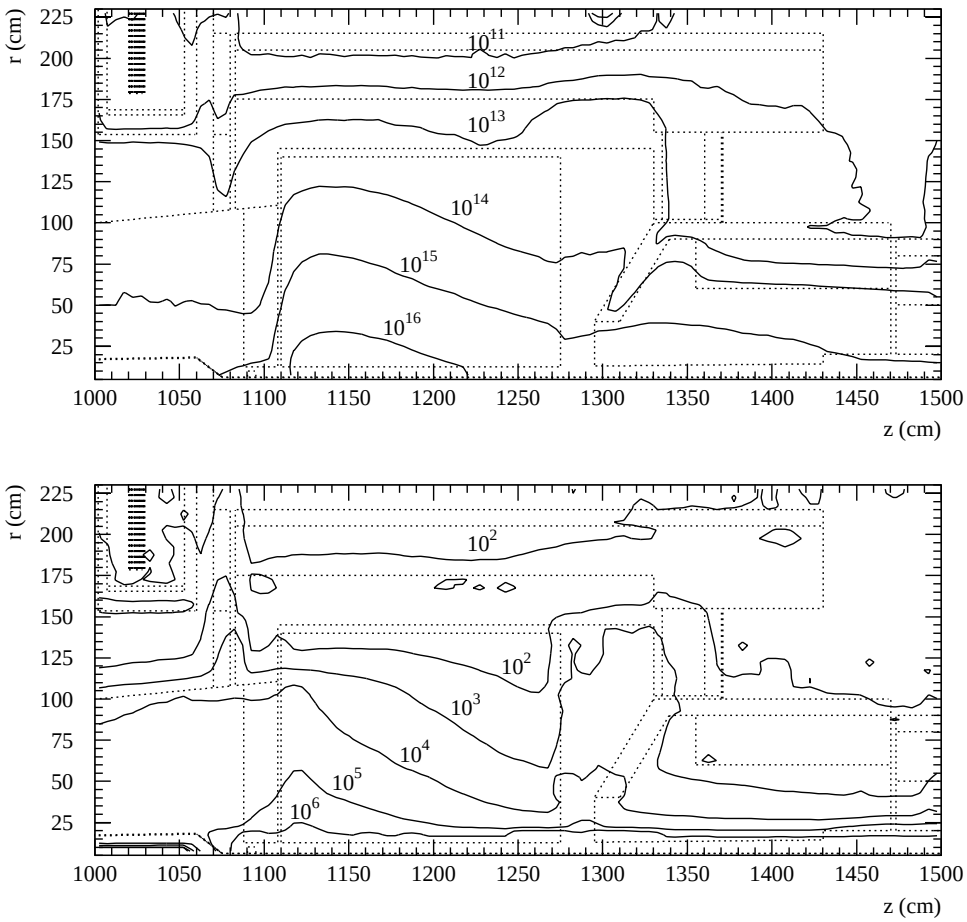

Figure 3: Fluence of hadrons (E>100 keV) in $\mathrm{cm}^{-2}\mathrm{s}^{-1}$ (upper plot) and radiation dose in Gy (lower plot) in the HF and its surroundings. The dose plot has been smoothed by taking running averages of the values, which slightly masks the dependence of dose on geometry details. Values are given for $5 \times 10^5\,\mathrm{pb}^{-1}$.

1.8 Estimate of induced radioactivity

**** Still incomplete... hopefully finished within next two days ! ****

At LHC we will be confronted with two main mechanisms which create radioactivity in materials: low energy neutron activation and inelastic hadronic interactions at high energy.

Of these the latter is found to dominate, unless the choice of materials is very unfortunate with respect to neutron activation. Since, in addition, the most significant neutron activation channels are in the thermal energy range, which at LHC will not be dominant, we can devote most of our attention to high energy activation.

A proper treatment of induced radioactivity would require to first establish a full inventory of all created radionuclides and then to follow the time dependence of this set of nuclides. In copper we would need to

consider of the order of 50 radioisotopes in order to properly cover a time span between 10 minutes and 20 years. Since the production rate of each individual isotope will depend on the irradiation conditions and the irradiated material, i.e. on the exact position within the CMS system, the computing problem would grow to an enormous size.

Work is in progress to establish full radionuclide inventories in the most important locations and materials, but results are not yet available.

In order to establish the best estimate possible for the time being, we use the concept of ω-factors. These are based on the fact that with some 50 contributing nuclides, effects due to individual ones are averaged out so that the rate of inelastic hadronic interactions (stars) in the material is directly proportional to the gamma emission rate from that material due to the activity induced in it. These emitted gammas then also have to represent the true photon spectrum in an average way. This average treatment suggests that also the half-life of the dose rate ($\dot{D}$) could be parametrized. Indeed such a parametrization is provided by the Overton-Sullivan formula [12]

$$\dot{D} \sim \Phi \ln \frac{t_i + t_c}{t_c},$$

where t_i is the duration of the irradiation, t_c is the time since the end of the irradiation and Φ is the activating hadron fluence. Since the assumption that the averaging is valid implies that the emitted photon spectrum is time independent, the Overton-Sullivan formula can also be interpreted as a time dependence of the induced activity. A plot of this time dependence for the assumed LHC operating schedule is shown in Fig. 4. We clearly see the three 60-day operating periods per year, separated by 14 day stops and followed by a longer shutdown. It must be emphasized that the dose during irradiation is quite artificial, and its value depends strongly on the selection of the cooling time. One hour is chosen to represent a realistic delay between stopping of the machine and entering the CMS area. The most important observation is that after the fast drop during the first day of cooling, a further decrease of induced radioactivity is very slow. Except for the low luminosity start up phase the dose rate at any instant of time is within a factor of three from the dose rate scaled to t_i=60 days and t_c=1 day. In addition this scaling provides the best value for an access a few days after machine stop when LHC has been operating long enough so that the saturation level of activity has been reached.

All these apparently very rough methods are fitted and relatively well established for target materials of medium atomic weight. Thus they are well suited for iron, steel and copper, but should not be applied to light materials like aluminium. An additional limitation is that the methods have been verified only for half lives between 10 minutes and 10 years and their validity outside this range is highly questionable.

A typical value for the ω-factor in iron or copper is 10^{-8} (Sv h^{-1})/(star cm^{-3} s^{-1}). Thus the star density production rate multiplied by the ω-factor gives the dose equivalent rate. But the value obtained is defined to be in contact with a semi-infinite slab of uniformly activated material. For the relatively small objects and highly non-uniform irradiation, which we encounter at CMS, this is a severe restriction. In particular ω-factors themselves do not give the dose at a distance from the activated object.

A ray-tracing method to calculate the dose rate at any given position in an activated environment is implemented in the FIASCO-code [13], which is a subroutine package to be used with FLUKA. The code uses as its input the star densities calculated with FLUKA and latest fits of the ω-factors, but converted to Bq/star factors. The ω-factors used in FIASCO are by a factor of 2-3 lower lower than the classical values. The difference arises from the fact that the older values have been obtained with simulation codes with less complete physics, i.e. less stars. Other effects are due to the accurate buildup model in FIASCO, which increases the estimated penetration compared to rougher calculations.

Thus 10^{-8} (Sv h^{-1})/(star cm^{-3} s^{-1}) is a proper value for fast estimation of dose equivalent rate in contact

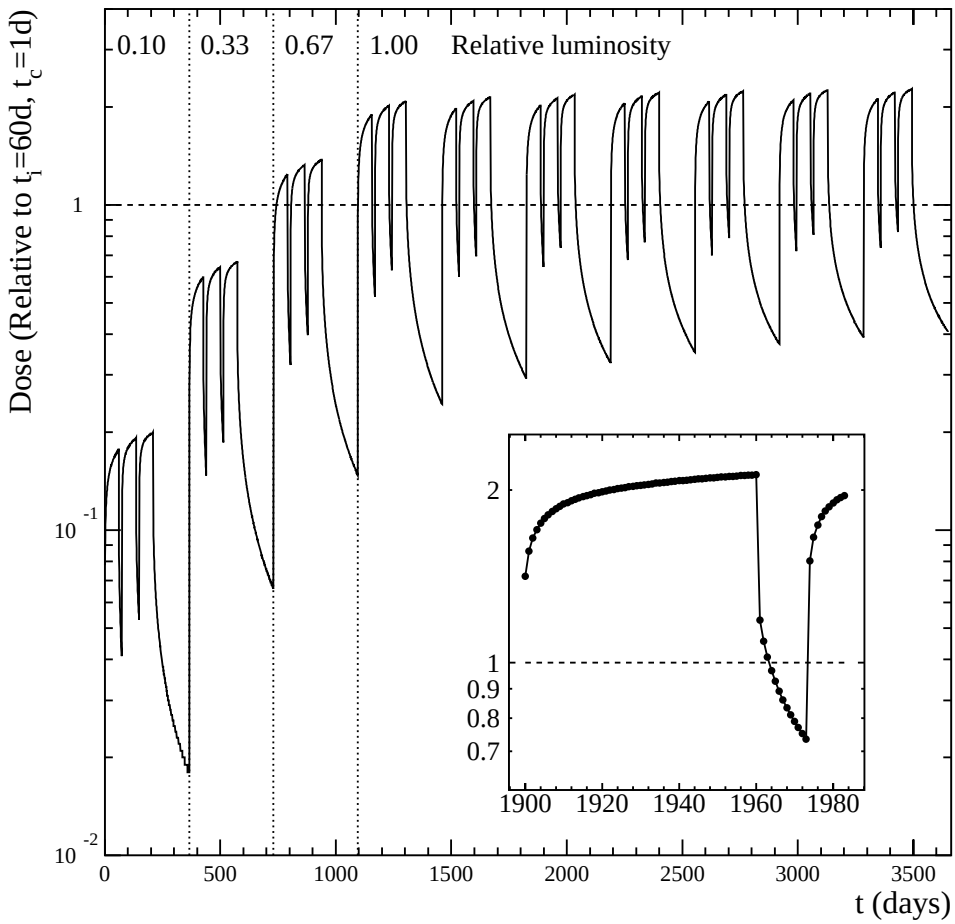

Figure 4: Time variation of induced activity dose rate at LHC according to the Overton-Sullivan formula. The curve is normalized such that unity (dashed line) coincides with t_i=60 days and t_c=1 day and the maximum average luminosity of LHC (5×10^{33} cm^{-2}s^{-1}). This corresponds to the scaling which is used to present the dose rates in Fig. 5. The heavy ion operation has been neglected. In the small sub-plot the dots indicate individual days.

(**** picture to come ****)

Figure 5: Estimated dose rate in μSv/h around the HB/HE and around the HF due to induced radioactivity. The values are plotted for an irradiation time of 60 days and a cooling time of 1 days (see Fig. 4). The average luminosity during the irradiation is assumed to be 5×10^{33} cm^{-2}s^{-1}.

with activated iron or copper, but it is expected to provide always upper estimates with respect to realistic cases.

More accurate estimates are provided in Fig. 5 where the dose rates, as calculated with FIASCO, due to induced activity close to the HB/HE and around the HF are shown. Other subdetectors and activated elements, in particular the EE and the beam pipe, have been excluded from the calculation.

z (cm)	$\eta = 1.5$	$\eta = 2.0$	$\eta = 2.8$
388	570	3800	24000
397	330	2900	26000
406	220	1900	19000
414	160	1300	13000
423	130	870	10000
432	67	520	7000
441	43	360	5800
450	22	250	4400
458	13	170	3500
467	8.1	120	2900
476	7.1	67	2500
485	3.4	57	2400
494	3.7	37	1900
502	0.94	24	1600
511	0.63	21	1300
520	0.42	11	1400
529	0.36	6.6	1100
538	0.12	5.0	950
546	0.40	5.8	810
555	0.52	11	990

Table 2: Radiation dose (Gy) in the scintillators of the HE for an integrated luminosity of $5 \times 10^5 \text{pb}^{-1}$. (**** I would propose to keep only some of the z-value in this table ****)

2 Radiation levels in scintillators

(**** This text is intended for use in some dedicated chapter if needed ****) (**** Requests for additions or changes are wellcome ! ****)

In Tab. 2 the dose in the HE scintillators is collected along lines of constant rapidity. The raw data is obtained from equidistant radial bins and the values have been linearly interpolated between two bins. Corresponding data for the HB is shown in Tab. 3. It has to be emphasized that the statistical significance of the given dose values in the outermost corner if the HE, around η=1.5, is relatively poor.

We observe an increase of dose in the last scintillator layer. This is mostly due to the close by slot for the endcap muon station ME1/1. The maximum dose at η=2.8 is 26 kGy. Going even further up in pseudorapidity, the absolute dose maximum of 37 kGy is found in the second scintillator layer of the HE (after first absorber plate) at a radius of 40-45 cm.

The alternating absorber/scintillator structure of the HCAL affects also the neutron spectrum locally. In the plastic the neutrons are efficiently moderated, whereas most of them are produced in the absorber. But since the plastic layers are relatively thin, it is justified to give the energy-integrated neutron fluence independent of the detailed calorimeter structure. Therefore the neutrons were scored in a 2×2 cm^2 binning, covering all of the calorimetry. Tabs. 4 and 5 show the obtained results along the selected η-lines. In addition to the total fluence, the neutron fluence above the 'silicon damage threshold' of 100 keV is shown separately.

The general "rule of thumb" that in hydrogen containing regions of CMS the 100 keV threshold roughly splits the total neutron fluence in half, gets further verification from these HCAL fluences.

Radius (cm)	$\eta = 0.1$	$\eta = 0.6$	$\eta = 1.1$
198	190	250	300
204	130	140	210
210	94	84	130
216	63	64	74
221	51	53	58
227	38	30	44
233	27	19	23
239	17	14	18
244	12	11	14
250	7.1	6.6	11
256	5.3	5.1	8.1
261	4.8	4.3	5.2
267	2.7	2.2	4.6
273	2.7	2.5	3.3
279	1.7	1.8	3.2
284	0.93	1.3	1.9
292	0.76	0.98	1.7

Table 3: Radiation dose (Gy) in the scintillators of the HB for an integrated luminosity of $5 \times 10^5 \text{pb}^{-1}$. (**** I would propose to keep only some of the r-values in this table ****)

Activation and associated gamma production are mainly low-energy phenomena, usually occurring only in the thermal regime. It should be understood that the actual thermal neutron fluence is only a small fraction of the difference between the total and the $>$100 keV fluence. In most parts of the HCAL the thermal neutron fluence is less than one percent of the total. But it should be noted that this low fluence is mostly due to the relatively small range of thermal neutrons in the HCAL material.

3 Radiation levels in HPD boxes

The HPD boxes were included explicitly in the simulation, although modelling them as an annular ring in order to preserve the cylindrical symmetry. Their average density was assumed to be 2.4 g/cm^3. The composition was assumed to be a copper/plastic mixture.

Tab. 6 shows the particle fluences and radiation dose in the barrel and endcap HPD boxes.

It can be seen that the radiation levels are higher in the barrel, where the absorber thickness is smaller than in the endcap. Compared to the values along the η=1.1 line in Tab. 5 the neutron fluence in the barrel HPD box appears slightly higher. This effect is caused by the fact that the η=1.1 line does not cross the box, but is contained deeper inside the HB material. The box is openly exposed to the HB/HE crack, where we have slightly higher fluences due to radiation streaming.

Fig. 6 shows the photon and neutron spectra in the barrel HPD box. The spectra in the endcap box are very similar and therefore not shown. It is evident that almost all observed photons are generated locally, mostly by neutron capture. This also explains the sharp drop of the photon flux at energies above 10 MeV.

z (cm)	$\eta = 1.5$		$\eta = 2.0$		$\eta = 2.8$	
	All	$E_n > 100\,\text{keV}$	All	$E_n > 100\,\text{keV}$	All	$E_n > 100\,\text{keV}$
393	1900	1100	10000	6600	48000	33000
403	1300	780	10000	6100	56000	36000
413	940	480	8200	4500	49000	29000
423	580	290	5300	2600	40000	22000
433	330	170	3700	1900	32000	17000
443	220	120	2300	1200	24000	14000
453	130	78	1500	850	20000	12000
463	74	42	980	570	16000	9800
473	49	26	620	350	15000	8500
483	32	16	440	240	12000	6700
493	18	8.9	280	130	10000	5100
503	11	4.9	180	92	9400	4700
513	5.8	2.9	110	58	8100	4300
523	3.5	1.6	68	37	7100	4100
533	2.0	1.1	46	26	6200	3200
543	2.4	0.88	48	28	5400	3100
553	5.9	2.9	56	25	6600	3600

Table 4: Neutron fluence (total and $E_n > 100\,\text{keV}$) in the HB. Values are given in 10^{10} neutrons per cm^2 for and integrated luminosity of $5 \times 10^5 \text{pb}^{-1}$.

Radius (cm)	$\eta = 0.1$		$\eta = 0.6$		$\eta = 1.1$	
	All	$E_n > 100\,\text{keV}$	All	$E_n > 100\,\text{keV}$	All	$E_n > 100\,\text{keV}$
198	1400	500	1600	640	1900	800
208	630	290	700	320	890	430
218	310	180	340	200	520	280
228	150	73	200	100	250	130
238	94	47	110	51	150	66
248	55	24	49	24	79	40
258	31	18	35	21	53	26
268	17	10	22	12	31	15
278	12	5.7	14	5.8	16	7.8
288	8.4	4.4	8.6	3.6	12	6.2

Table 5: Neutron fluence (total and $E_n > 100\,\text{keV}$) in the HB. Values are given in 10^{10} neutrons per cm^2 for and integrated luminosity of $5 \times 10^5 \text{pb}^{-1}$.

4 HF Shielding requirements and constraints

**** The following is for chapter 5.4 *****

**** final figures of shielding to come from engineers ****

The large amount of hadronic energy absorbed in the HF inevitably leads to the generation of an immense neutron flux inside of the HF. We observe substantial hadronic leakage from the rear face even after 10 interaction lengths. Fortunately most of the punchthrough is contained within the shielding or is directed towards the end wall of the cavern and does not directly hit any other subdetector. Some of these particles

	Barrel	Endcap
Total neutron fluence	28	7
Hadron fluence	13	2
Photon fluence	9	2
Dose	1.6	0.2

Table 6: Particle fluence and dose in the HPD boxes. The hadron fluence is mainly neutrons above 100 keV and is the proper quantity for estimating silicon bulk damage. All fluences are given in 10^{10} cm^{-2} and the dose in Gy. All values are for 5×10^5 pb^{-1}.

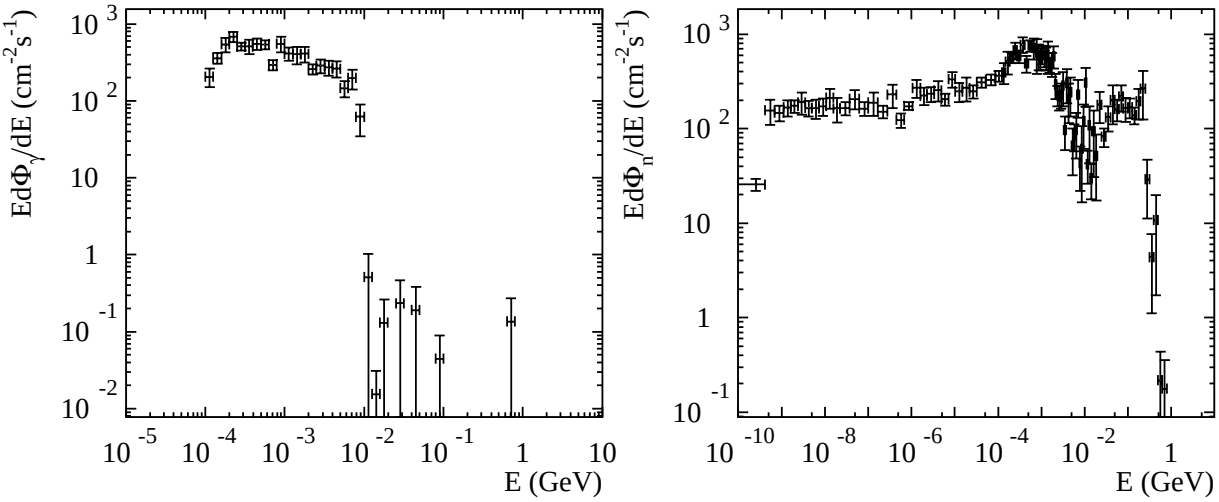

Figure 6: Energy spectra of photons and neutrons in the barrel HPD box. Values are for LHC peak luminosity

will cross the photomultipliers and front-end electronics. The protection of these devices is the primary reason for quite substantial shielding at the back of the HF. This shielding is also useful for the endcap muon system, since the energy carried by the punchthrough particles is converted into neutron and photon albedo at the end wall of the experimental hall, and so indirectly influences ME4.

For ME4, radial leakage from the HF is more of concern than punchthrough. Particles emerging from the HF side faces could directly impinge on the CMS endcap. A substantial effort has been recently devoted to optimizing the shielding configuration around HF.

The neutron albedo from the HF front face has been shown to be of no importance for the central tracker but, if unshielded, would be an important source of background in the high-η region of the endcap muon spectrometer. A 20 cm thick polyethylene slab lining the HF front face is sufficient to suppress the neutron albedo below the level of the neutron flux generated by interactions in the beam pipe.

An important channel for neutron leakage from the HF directly into ME4 has been blocked by introduc-

	FLUKA	MARS
All neutrons	2.8×10^{12}	—
Neutrons E>100 keV	2.3×10^{12}	2.9×10^{12}
Thermal neutrons	8.3×10^{9}	—
Charged hadrons	3.8×10^{10}	2.0×10^{10}
Dose	90	—

Table 7: Particle fluences (in $cm^{-2}s^{-1}$) and radiation dose (in Gy) in the position of the photomultipliers of the HF. Values are given for 5×10^5 pb^{-1}.

ing a 10 cm thick borated polyethylene slab into the endcap/HF interface. The interface itself is designed to be flat, with a clearance not exceeding 3 cm. The lateral faces of the HF are surrounded by 70 cm of shielding, of which the innermost 30 cm are steel followed by 30 cm magnetite concrete (density 3.65 g/cm^3). The shielding is finished off with a 10 cm thick layer of borated polyethylene. In addition to some weight saving, it is of advantage to make this shielding close to cylindrical. A shielding with square cross section would leave in the corners some parts of ME4 directly exposed to the HF.

At the back of HF we have to deal with the interface to the rotating shielding and with the issue of accommodating and shielding the photomultipliers. The inner radius of HF is assumed to be 12.5 cm. Behind HF we have a relatively massive shielding block starting at z=12.95 m. The inner boundary of this block is conical and follows the η =5.31 line. The block has an outer radius of 100 cm and consists of steel and magnetite concrete. Its outer surface is covered by 10 cm of borated polyethylene. The interface to the rotating shielding is provided by having the last 40 cm of this shielding block as a separate entity which would be inserted after both the HF including its shielding and the rotating shielding are in place. The crack between the HF shielding and the rotating shielding is shown to be critical. A flat connection is possible if the clearance does not exceed 3 cm. Assuming these 3 cm clearance, the rotating shielding starts at z=1496 cm. In addition to its main task of reducing the background in the experimental cavern and ME4, the thin section of the rotating shielding plays a non-negligible role in shielding the HF photomultipliers. The optimization of the rotating shielding design in view of ME4 is still in progress. Here we use the best design encountered so far, which consists of three radial layers: 30 cm steel starting at R=20 cm, followed by 30 cm of magnetite concrete and further 10 cm of borated polyethylene, giving an outer radius of 90 cm.

The photomultipliers are stacked between the cylindrical shielding block and the outer lateral shielding described above. To suppress the fluence of punchthrough particles, a special shielding consisting of 5 cm steel, 25 cm borated polyethylene and 10cm steel is placed between the HF and the photomultipliers. The fibres from the HF will be fed to the photomultipliers through small holes in this shielding. Support of the photomultipliers is in addition to the last 10 cm of shielding steel.

4.1 Results of radiation simulations

We have calculated the particle fluences and radiation dose in a glass plate representing the photomultiplier windows. The results are collected in Tab. 7 and the radial dependence of fluences and dose is shown in Figs. 7 and 8. Alongside the FLUKA results we provide some values obtained with the MARS code. In general we observe very good agreement. The increase of the MARS neutron fluence estimate with respect to FLUKA at large radii is probably explained by the significantly longer scoring bins (along z) used in MARS.

Fig. 9 shows the photon and neutron spectrum in the position of the photomultipliers. We observe that, as

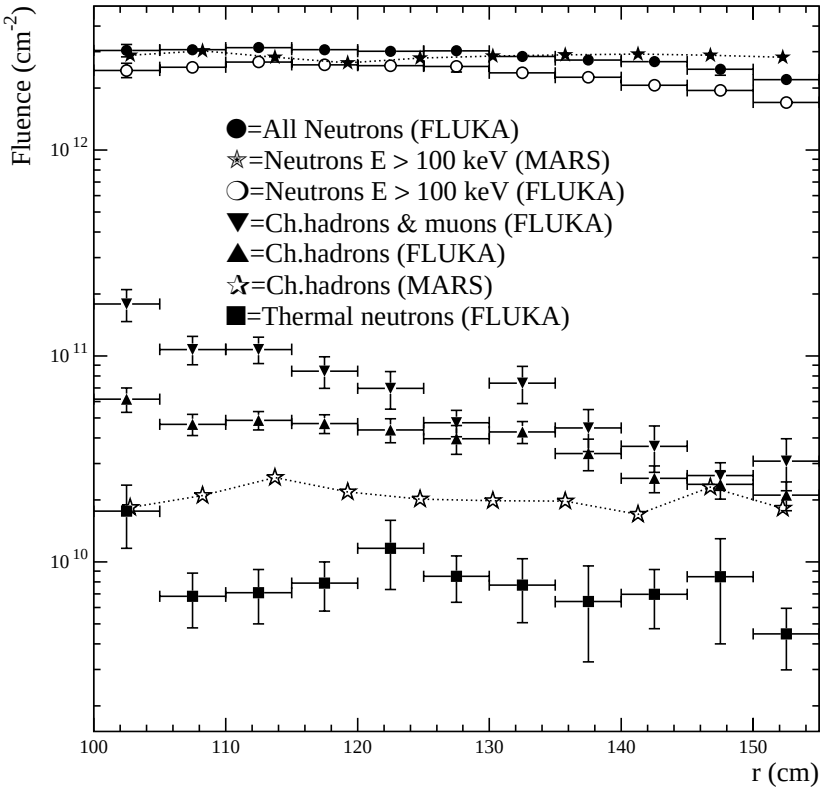

Figure 7: Fluence of different particle types in the position of the photomultipliers as a function of radius. Values are for 5×10^5 pb^{-1}.

expected, the polyethylene has removed a significant amount of the neutrons around 1 MeV and therefore lowered the potential bulk damage to silicon devices. When interpreting the photon spectra of Figs. 9, 11 and 14 it should be remembered that photons emitted in radioactive decays are not included in the simulation.

Figs. 8 and 10 show the dose and particle fluences as a function of radius just behind the HF absorber. We can observe a variation by several orders of magnitude between the innermost and outer radii.

Fig. 11 shows the photon and neutron spectrum just behind the HF absorber averaged between radii of 20 cm and 60 cm. The neutron spectrum shows the typical shape inside or on top of pure metal, with very few thermal neutrons (probably backscattered from the polyethylene on the shielding plug) and a very pronounced 1 MeV 'evaporation peak'. The smaller peak around 100 MeV is the more significant one, since these neutrons are very penetrating. Note that the increase of the absolute values with respect to Fig. 9 is not an effect of the polyethylene shielding of the photomultipliers alone, but mostly caused by the different radial range considered.

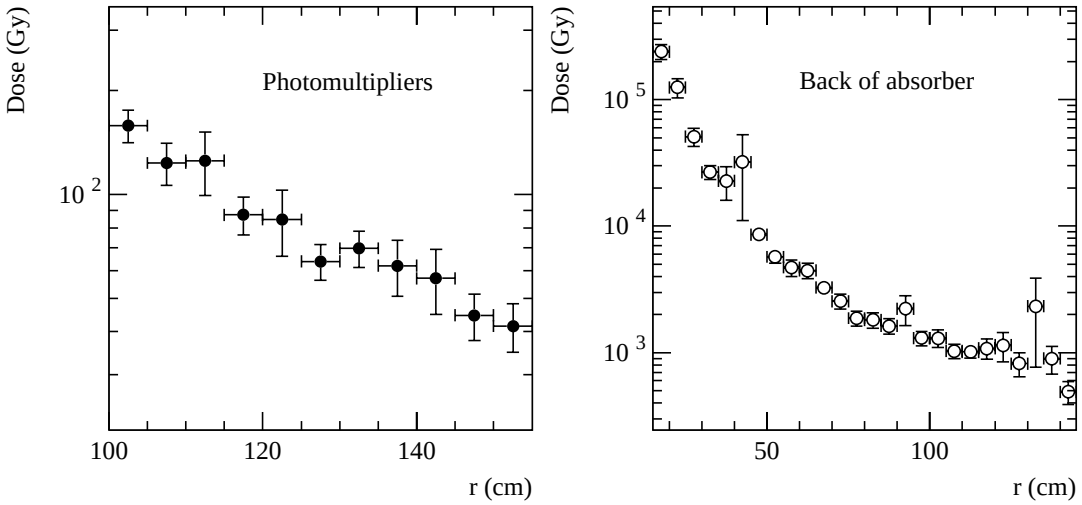

Figure 8: Radiation dose in the photomultiplier windows (glass) and just behind the absorber (air) as functions of radius. Values are for 5×10^5 pb^{-1}.

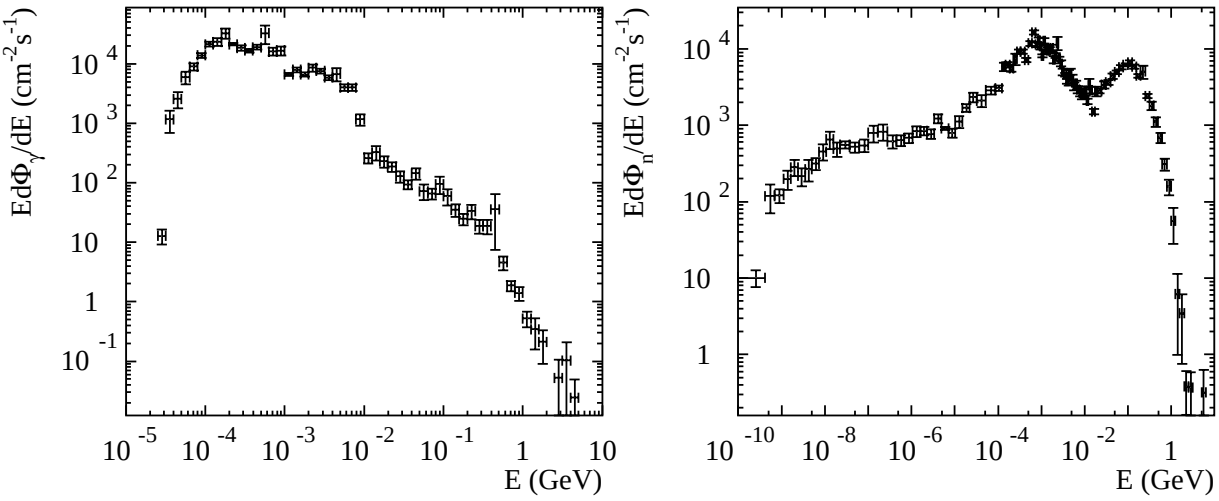

Figure 9: Energy spectra of particles in the position of the photomultipliers. Values are for LHC peak luminosity

One important issue is, where to place the electronics racks needed by the HF. Since the cable length from the photomultipliers to these racks has to be minimized, the most suitable position is just outside of the lateral shielding of the HF. Fig. 12 shows the fluence of different particle types in this position as a function of the longitudinal (z) coordinate. The large increase of fluence at z=1080 cm is caused by

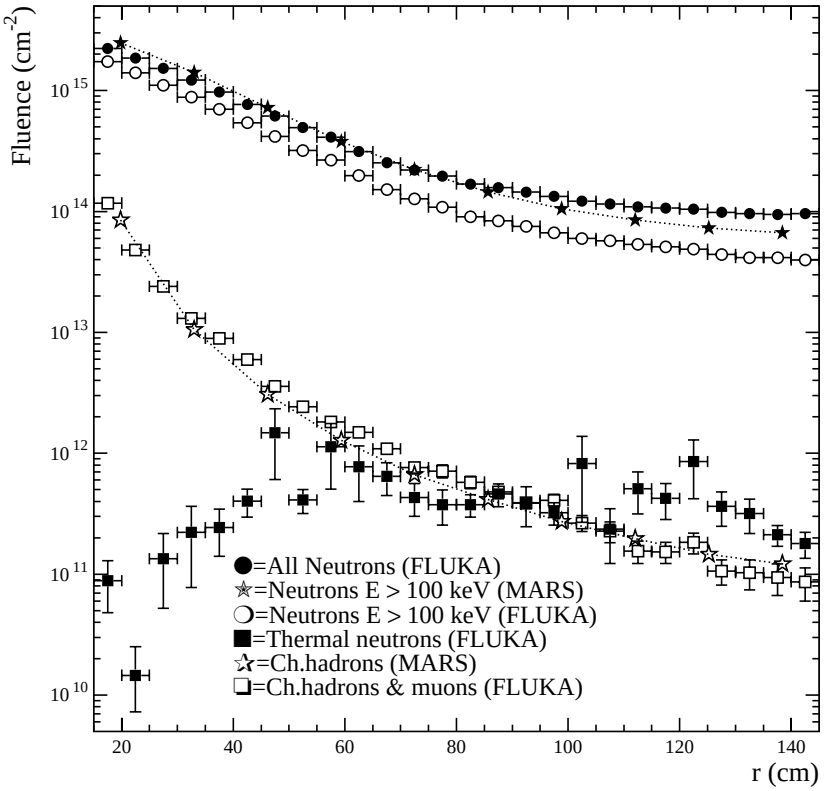

Figure 10: Fluence of different particle types just behind the absorber as a function of radius. Values are for 5×10^5 pb^{-1}. The muon contribution in the charged fluence, quoted for FLUKA, is only few tens of percent so the pure charged hadron curve would be almost indistinguishable from the presented one.

the 3 cm wide crack between the endcap and the HF shielding. An inspection of the curves shows that most of the bulk damage in silicon devices will be caused by neutrons with energies above 100 keV. The contribution by other hadrons is relatively small.

Radiation dose probably is the more important parameter for the electronics racks. The dose as a function of z is shown in Fig. 13. The dose just inside the borated polyethylene shielding is shown alongside the dose in the air just outside the shielding. As expected the dose in the polyethylene is higher, which can be attributed to recoils from (n,p) reactions. The dose in silicon itself should be close to that in air. But in the racks we can expect a certain amount of cables and other plastic items to accompany the silicon devices. Therefore the two values should provide a proper estimate of the uncertainty in dose due to the material composition of the racks.

Both the fluence and dose have a minimum between z=12 m and z=12.5 m which thus is the preferred position for the racks. Beyond z=13 m we observe a clear increase of fluences and dose, which is caused

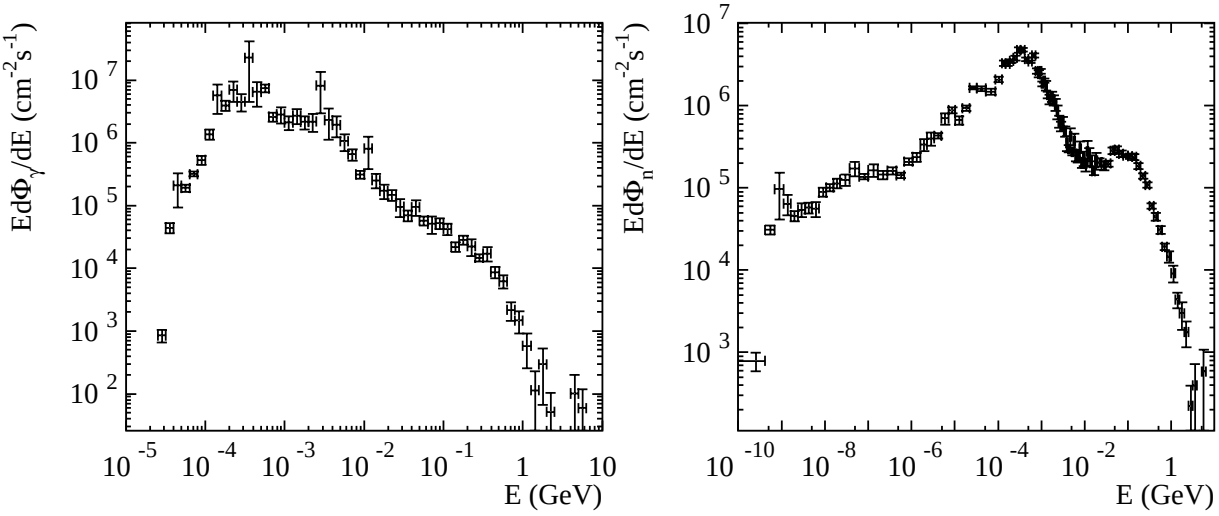

Figure 11: Energy spectra of particles just behind the HF absorber averaged over radii R=20 cm to R=60 cm. Values are for LHC peak luminosity

by the end of the absorber and the therefore significantly reduced lateral shielding.

Fig. 14 shows the energy spectra of photons and neutrons on top of the lateral shielding of the HF. While nothing unusual can be observed in the photon spectrum, the neutron spectrum is remarkably hard. The deficiency of thermal neutrons is explained by the borated polyethylene which forms the top part of the shielding. The fact that the 1MeV 'evaporation peak' has almost disappeared tells that the shielding provides very efficient neutron attenuation in the energy range where hydrogen is effective. The neutrons at about 100 MeV cannot be stopped, except with very massive shielding for which we have neither the space nor the possibilities of supporting.

References

[1] K. Potter and G. R. Stevenson, *Average interaction rates for shielding specification in high-luminosity LHC experiments*, CERN LHC Note 310 (1995).

[2] M. Hoefert, K. Potter and G. R. Stevenson, *Summary of design values, dose limits, interaction rates etc for use in estimating radiological quantities associated with LHC operation*, CERN TIS-RP/IR/95-19.1 (1995).

[3] J. Ranft, Phys. Rev. D51 (1995) 64.

[4] P. Aurenche et al., Computer Physics Commun. 83 (1994) 107.

[5] H. Bengtson and T. Sjöstrand, Computer Physics Commun. 43 (1987) 43.

[6] P. A. Aarnio *et al*, CERN TIS-RP/168 (1986) and CERN TIS-RP/190 (1987)
A. Fassò *et al*, Proc IV Int. Conf. on Calorimetry in High Energy Physics, La Biodola, Sept 20-25, 1993, Ed. A. Menzione and A. Scribano, World Scientific, p. 493 (1993).

[7] W. Nelson, H. Hirayama, D. Rogers, Report SLAC-265 (1985).

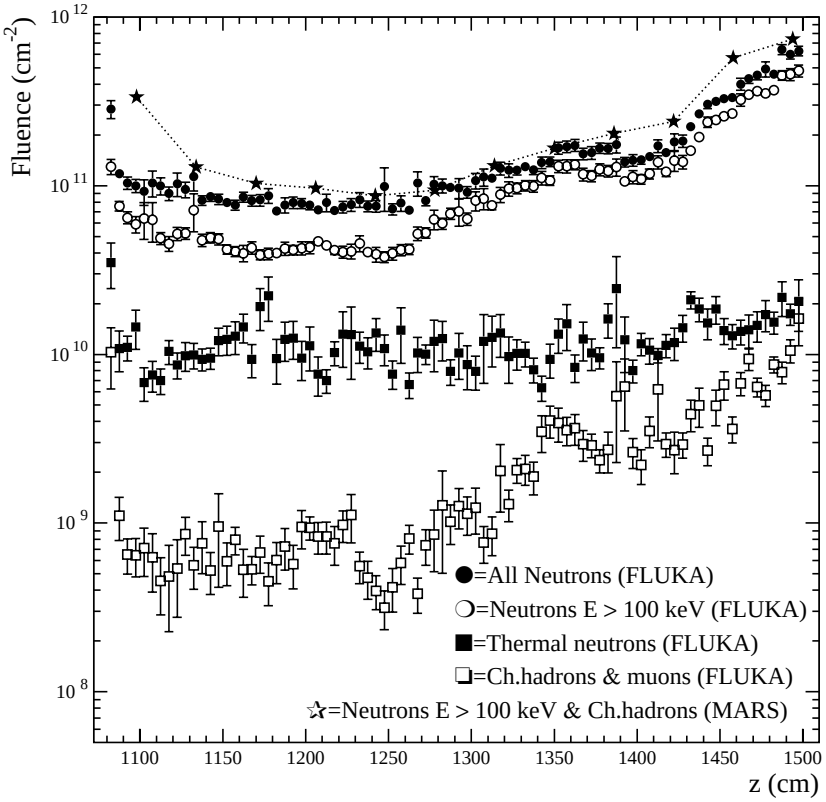

Figure 12: Fluence of different particle types on top of the lateral shielding of the HF as a function of z-coordinate. Values are for 5×10^5 pb^{-1}.

[8] M. Huhtinen and C. Seez, *Uncertainties in fluences and doses at the CMS inner tracker*, CERN CMS/TN 95-133.

[9] A. Fassò *et al*, Nucl. Instr. and Meth. A332 (1993) 459.
C. Birattari *et al*, Nucl. Instr. and Meth. A338 (1994) 534.

J. Ranft, *DPMJET-II, a Dual Parton Model event generator for hadron-hadron, hadron-nucleus and nucleus-nucleus collisions*, Presented at SARE2 workshop, CERN, 9-11 October, 1995, Proceedings: CERN/TIS-RP/97-05 (1997)

[10] M. Huhtinen, *Radiation environment simulations for the CMS detector*, CERN CMS TN/95-198 (1995), Presented at SARE2 workshop, CERN, 9-11 October, 1995, Proceedings: CERN/TIS-RP/97-05 (1997)

[11] M. Huhtinen, *Studies of neutron moderator configurations around the CMS inner tracker and ECAL*, CERN CMS TN/96-057 (1996).

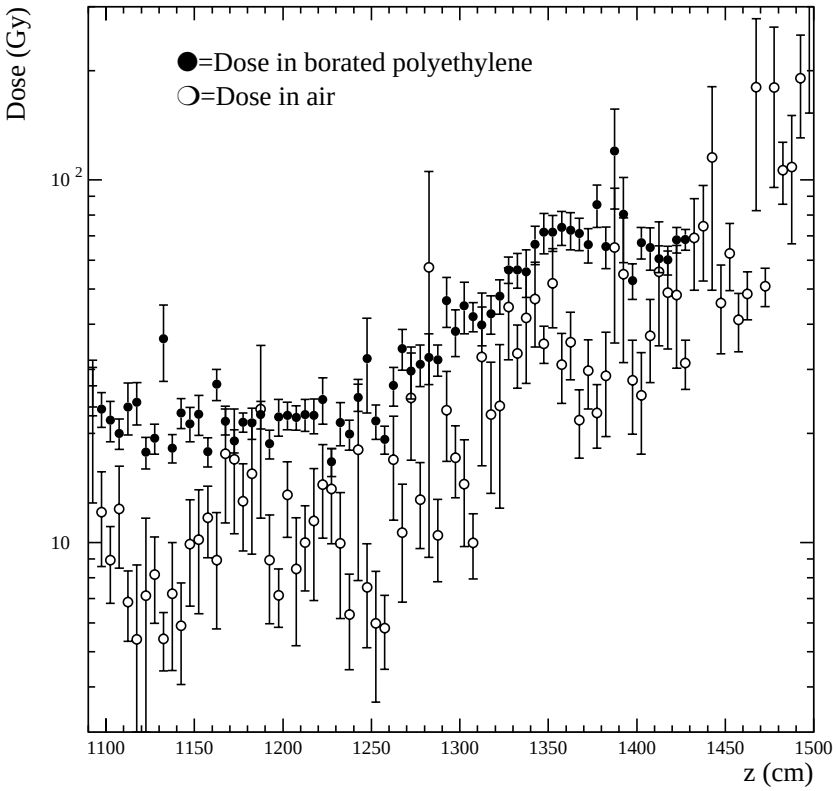

Figure 13: Radiation dose on top of the lateral shielding of the HF as a function of z-coordinate. The large error bars in the air values are caused by the low density, which reduces the number of energy deposition events. Values are for 5×10^5 pb^{-1}.

[12] A. Sullivan and T. Overton, Health Physics 11 (1965) 1101.

[13] M. Huhtinen, *Method for Estimating Dose rates from Induced Radioactivity in Complicated Hadron Accelerator Geometries*, to be published as CERN TIS Divisional Report (1997).

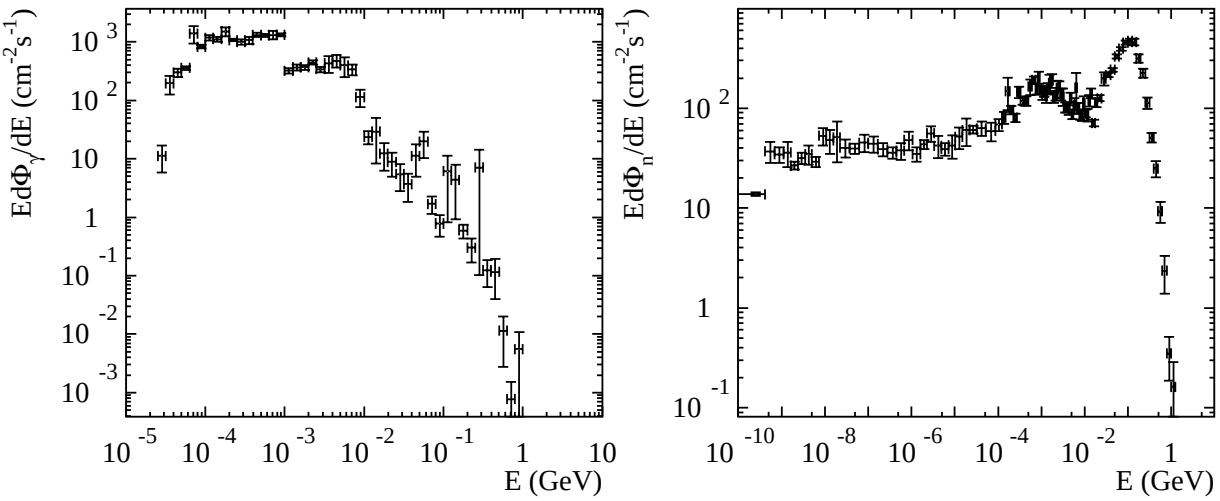

Figure 14: Energy spectra on top of the HF lateral shielding where electronics racks will be positioned. Values are for LHC peak luminosity.